

## Article

# Thermal Analysis of Power Converters for DFIG-Based Wind Energy Conversion Systems during Voltage Sags

Igor Rodrigues de Oliveira <sup>1</sup>, Fernando Lessa Tofoli <sup>2,\*</sup>  and Victor Flores Mendes <sup>1</sup> 

<sup>1</sup> Graduate Program in Electrical Engineering, Federal University of Minas Gerais, Belo Horizonte 31270-901, Brazil; igorrol@ufmg.br (I.R.d.O.); victormendes@cpdee.ufmg.br (V.F.M.)

<sup>2</sup> Department of Electrical Engineering, Federal University of São João del-Rei, São João del-Rei 36307-352, Brazil

\* Correspondence: fernandolessa@ufsj.edu.br

**Abstract:** The doubly fed induction generator (DFIG) and back-to-back converter are very sensitive to power quality disturbances in grid-connected wind energy conversion systems (WECSs). Special attention has been given to protect the system from voltage sags, considering the introduction of several low-voltage ride-through (LVRT) techniques in the literature. However, only few works have really analyzed the behavior of power semiconductors during such phenomena in terms of the thermal stresses, whereas the existing studies are focused on balanced voltage sags only. In this context, this work presents a thermal profile analysis of power semiconductors in the grid-side converter (GSC) and rotor-side converter (RSC) considering a DFIG-based WECS submitted to symmetrical and asymmetrical voltage sags. The system is modeled using PLECS software and results on a 2.0 MW system are presented and thoroughly discussed. The results show that it is possible to meet the ride-through requirements during both balanced and unbalanced sags in terms of acceptable thermal stresses on the semiconductors as long as the back-to-back converter and its respective control system are properly designed.



**Citation:** de Oliveira, I.R.; Tofoli, F.L.; Mendes, V.F. Thermal Analysis of Power Converters for DFIG-Based Wind Energy Conversion Systems during Voltage Sags. *Energies* **2022**, *15*, 3152. <https://doi.org/10.3390/en15093152>

Academic Editor:  
Charalampos Baniotopoulos

Received: 2 April 2022

Accepted: 25 April 2022

Published: 26 April 2022

**Publisher's Note:** MDPI stays neutral with regard to jurisdictional claims in published maps and institutional affiliations.



**Copyright:** © 2022 by the authors. Licensee MDPI, Basel, Switzerland. This article is an open access article distributed under the terms and conditions of the Creative Commons Attribution (CC BY) license (<https://creativecommons.org/licenses/by/4.0/>).

**Keywords:** DFIG; power semiconductors; thermal analysis; voltage sags; wind energy conversion systems

## 1. Introduction

Wind energy has become an interesting alternative toward the solution of the world-wide energy crisis. In 2020, the global installed capacity of wind power plants reached 93 GW, this being the best result ever [1]. Considering that wind energy conversion systems (WECSs) are widely used in grid-connected applications, they should not only be tolerant to the occurrence of faults, but also have the ability to support the grid during voltage transients. In this sense, it is worth mentioning that the back-to-back converter is often the most sensitive element subjected to such undesirable phenomena [2].

It is well known that the doubly fed induction generator (DFIG) is one of the most popular choices for WECSs because it allows the operation with variable speed [3]. It also has the advantages of providing active and reactive power control, whereas the rated power of the power electronic converter is only a fraction of the generator rated power, that is, generally between 20% and 30%. However, DFIGs are very sensitive to grid disturbances, especially to voltage sags. The abrupt drop in grid voltage causes overvoltages and consequently overcurrents in the rotor windings, which could even destroy the converter if no protection systems are included [4,5]. WECSs must also comply with grid code requirements, among which low voltage ride through (LVRT) is of particular interest. Since 2003, the Brazilian Electric System Operator (ONS) stated that WECSs must incorporate the ability to maintain the operation without interrupting the power supply during abnormal conditions of the grid voltage [6]. In a recent revision in 2019, the grid code also incorporated the necessity of injecting reactive power to support the grid during faults or voltage dips.

During the last decade, several works proposed different strategies to improve the LVRT capability of DFIGs. LVRT techniques can incorporate additional hardware into the system such as crowbars, DC choppers, series dynamic resistors (SDRs), and DC-link energy storage systems (ESSs) [7–11]. They can also use control strategies to improve the overall dynamic performance, this being a more cost-effective solution that does not require additional devices. In this sense, many advanced control techniques have been proposed in the literature, which are briefly discussed as follows [12–20].

The authors in [13] propose a control system capable of emulating the insertion of an inductance into the rotor-side converter (RSC) during voltage sags. This strategy presents good tradeoffs between the high currents and high voltages required by several methods. However, the rotor currents still reach high values when severe voltage sags occur and it is not possible to inject reactive power during the fault. The follow-up study in [14] proposes some improvements with regard to the well-known proportional-integral (PI) control of negative- and natural-sequence components by means of feedforward control of the oscillating components. The method is not intended for optimizing the current limiting or protecting the converter, but dampening the oscillations caused by traditional control approaches instead. A feedforward transient control (FFTC) scheme is proposed in [15], which introduces additional feedforward transient compensation to a conventional current regulator. When a three-phase fault occurs, these compensation terms correctly align the output voltage of the RSC with the induced transient voltage, resulting in minimum transient rotor currents and minimum occurrence of crowbar interruptions. However, the computational burden is higher when compared with conventional controllers.

Some works have proposed distinct controllers for improving the DFIG performance based on real-time implementation. For instance, a neural discrete-time inverse optimal controller (NNDTIOC) is introduced in [17]. The proposed scheme is the first one to use the optimal inverse control for trajectory tracking in a DFIG, also providing robustness to unmodeled dynamics and parameter variations with a neural network trained online. Classical current controllers based on the synchronous reference frame are not capable of providing very good performance under unbalanced voltage sags owing to the narrow bandwidth of PI controllers. A proportional current control with first-order low-pass filter disturbance observer (DOb) was then proposed in [18], establishing an independent control of both positive- and negative-sequence current components under asymmetrical grid voltage conditions. A model predictive control technique is described in [19], which relies on an effective linearized technique, i.e., the input–output feedback linearization method. The control law is derived from the optimization of two targets that aim to eliminate the oscillations in the active or reactive power. An advanced transient voltage control (A-TVC) solution is proposed in [21] to enhance the LVRT capability of the DFIG. This work assesses the system considering distinct sags levels while employing the aforementioned strategy to improve the transient voltage stability, as well as reducing the stator and rotor overcurrents. The authors in [22] present the modified super twisting (MST) algorithm for providing the system with an LVRT capability. This technique uses the second-order sliding mode (SOSM) approach to control the DFIG. The results show that this is an efficient method, but the study lacks a more in-depth analysis regarding more severe voltage sags. A magnetizing current control (MCC) scheme for DFIGs during symmetrical voltage sags is proposed in [23,24]. However, for severe voltage sags, there are still high currents flowing through the rotor. Therefore, this solution may only be effective when combined with other strategies.

Several LVRT approaches have been proposed in the literature, which comprise distinct advantages and disadvantages. Considering that the back-to-back converter is particularly sensitive to grid disturbances, significant effort has been recently devoted to ensure the reliable operation of power semiconductors owing to high cost and long maintenance periods after failures [25,26]. Notably, the thermal profile is an important indicator of the lifetime of semiconductors, with significant influence on the reliable system operation [27,28]. The number of energy cycles and the average junction temperature are very important aspects that do affect the junction temperature fluctuation [29–31].

Some works focused on evaluating the thermal behavior of power devices are reported in [27,28,32]. However, there is still a lack of studies that evaluate LVRT strategies from the perspective of the thermal profile of semiconductor devices when they are subjected to balanced and unbalanced voltage sags. The gap is even higher in relation to unbalanced dips. To the best of the authors' knowledge, no works on this subject could be found in the recent literature.

Considering these aspects, this work aims to present an analysis of power semiconductors used in DFIG-based WECSs submitted to balanced and unbalanced voltage sags. The main contribution of this work lies in carrying out an analysis of the thermal stresses on power semiconductors during such phenomena, in addition to deriving an adequate design approach for the power converter to ensure the safe operation of the whole system. For this purpose, a 2.0-MW WECS is assessed in detail using PLECS software, considering that the study presents a discussion of the involved quantities from the thermal point of view. The control loops associated with the negative-sequence components are also investigated.

The remainder of this work is organized as follows. Section 2 presents the structure of a DFIG-based WECS, as well as a brief explanation. Section 3 assesses the DFIG behavior when submitted to balanced and unbalanced voltage sags, as well as a negative-sequence control approach. Section 4 describes the thermal modeling of power semiconductors in terms of the design of insulated gate bipolar transistors (IGBTs) used in a 2.0-MW WECS simulated in PLECS software. Section 5 presents the discussion of results, whereas Section 6 concludes the study.

## 2. Overview of DFIG-Based WECSs

The basic structure of a DFIG-based WECS is shown in Figure 1. The system comprises the wind turbine, a gearbox, and the DFIG, which allows one to obtain variable-speed operation. The back-to-back converter consists of the RSC and the grid-side converter (GSC) connected to a low-pass filter for injecting power into the AC grid. A brief description of each aforementioned component is provided as follows.

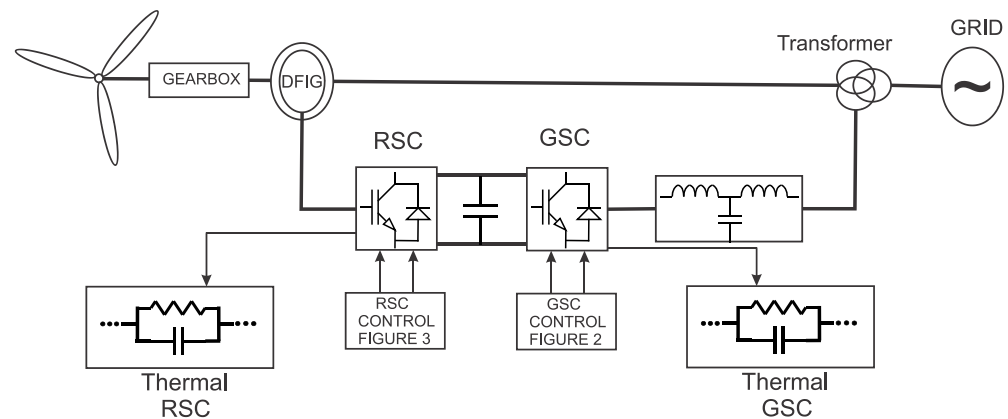


**Figure 1.** DFIG-based WECS.

### 2.1. DFIG

DFIGs convert the mechanical power generated by the turbine into electrical power injected into the grid by the stator and rotor windings. The rotor windings are connected to an AC/DC/AC power electronic conversion system and the stator windings are directly connected to the mains. The stator and rotor differential equations in the synchronous reference frame are defined in [33] as:

$$\vec{v}_s = R_s \vec{i}_s + \frac{d\vec{\psi}_s}{dt} + j\omega_s \vec{\psi}_s \quad (1)$$

$$\vec{v}_r = R_r \vec{i}_r + \frac{d\vec{\psi}_r}{dt} + j\omega_r \vec{\psi}_r \quad (2)$$

where the variables and the parameters are referred to the stator. The subscripts  $s$  and  $r$  refer to the variables and parameters of the stator and rotor, respectively;  $v_s$  and  $v_r$  are voltages;  $i_s$  and  $i_r$  are currents;  $\omega_s$  and  $\omega_r$  are angular frequencies;  $\psi_s$  and  $\psi_r$  are flux linkages; and  $R_s$  and  $R_r$  are resistances.

The stator and rotor flux linkages  $\psi_s$  and  $\psi_r$  are given by [33]:

$$\vec{\psi}_s = L_s \vec{i}_s + L_m \vec{i}_r = (L_{\sigma s} + L_m) \vec{i}_s + L_m \vec{i}_r \quad (3)$$

$$\vec{\psi}_r = L_r \vec{i}_r + L_m \vec{i}_s = (L_{\sigma r} + L_m) \vec{i}_r + L_m \vec{i}_s \quad (4)$$

where  $L_s$  and  $L_r$  are self-inductances;  $L_{\sigma s}$  and  $L_{\sigma r}$  are leakage inductances; and  $L_m$  is the magnetizing inductance.

According to [33], the differential equation that describes the mechanical system is:

$$J \frac{d\omega_m}{dt} + k_f \omega_m = T_e - T_{mec} \quad (5)$$

where  $J$  is the inertia moment of the mechanical system composed of the wind turbine and the generator;  $k_f$  is the friction coefficient;  $T_{mec}$  is the mechanical torque in the generator axis provided by the wind turbine through the gearbox; and  $T_e$  is the machine electromagnetic torque calculated from [33] as:

$$T_e = \frac{3}{2} p \frac{L_m}{L_s} \Im m \left\{ \vec{\psi}_s \vec{i}_r^* \right\} \quad (6)$$

where  $p$  is the number of poles of the machine and the superscript “ $^*$ ” denotes the complex conjugate.

## 2.2. AC/DC/AC Converter

The AC/DC/AC converter, that is, the back-to-back converter consists of two voltage-source converters (VSCs) connected to each other through a DC link. This topology often employs IGBTs driven by pulse width modulation (PWM) schemes. The RSC is connected to the rotor windings and is responsible for controlling the rotor currents. By means of the magnetic coupling with the stator circuit, it modifies the stator currents, also controlling the stator active and reactive powers. The GSC is connected to the grid through a low-pass filter that minimizes the harmonic content injected by the converter, also controlling the DC-link voltage and the reactive power flow. Conventional control approaches applied to the back-to-back converter often rely on vector control using the synchronous reference frame.

The classical control strategy uses internal loops for controlling the grid currents, which are oriented according to the grid voltage angle. This orientation allows the decoupled control of active and reactive powers [34]. The DC-link voltage control loop is external to the control loop associated with the direct ( $d$ ) axis current component, because this latter quantity is responsible for regulating the active power. The reactive power is regulated by a controller external to the loop associated with the quadrature ( $q$ ) axis current component. A block diagram representation of the GSC control can be seen in Figure 2.



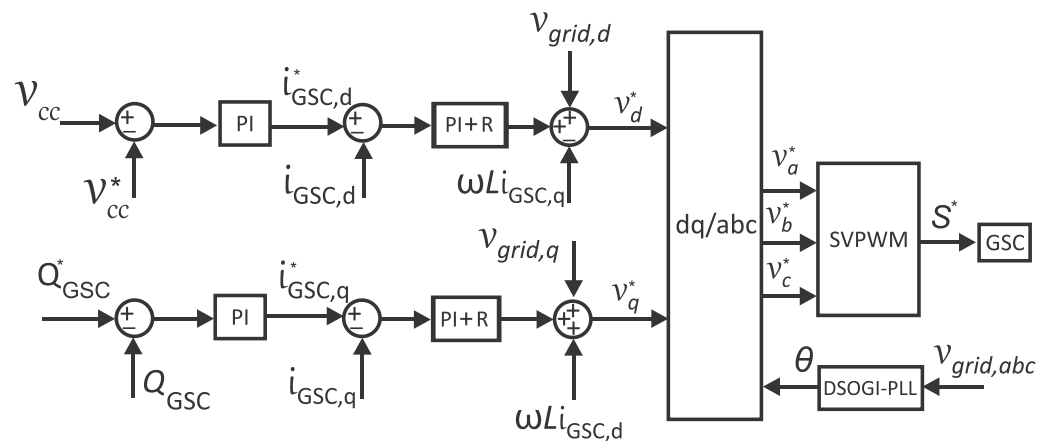


**Figure 2.** Block diagram representation of the GSC control structure.

According to Figure 2, the angle of the grid voltage vector  $\theta$ , which is used in the orientation of the converter currents, is estimated using a phase-locked loop (PLL). In this work, the dual second-order generalized integrator (DSOGI) was adopted for this purpose, whereas a detailed description can be found in [35]. The GSC is responsible for keeping a constant DC-link voltage, thus allowing the RSC to regulate the rotor currents as a consequence.

Considering the orientation of the stator voltage angle in accordance with the grid voltage, the stator active and reactive powers are calculated as [36]:

$$P_s = \frac{3}{2} v_{s_d} i_{s_d} = -\frac{3}{2} \frac{L_m}{L_s} v_{s_d} i_{r_d} \quad (7)$$

$$Q_s = -\frac{3}{2} v_{s_d} i_{s_q} = \frac{3}{2} \frac{v_{s_d}^2}{\omega_s L_s} + \frac{3}{2} \frac{L_m}{L_s} v_{s_d} i_{r_q} \quad (8)$$

The stator active and reactive powers depend on the  $d$  axis and  $q$  axis components of the rotor current, respectively. Therefore, decoupled inner current control loops associated with outer power control loops are used in the RSC as represented in Figure 3. The gains of the PI controllers used in RSC and GSC were obtained using the pole allocation method, as described in [37].

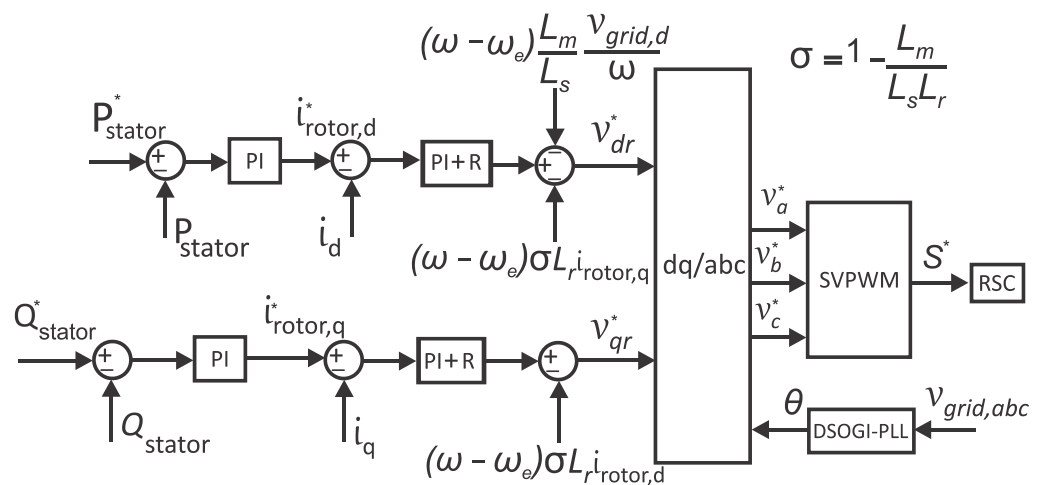


**Figure 3.** Block diagram representation of the RSC control structure.

Based on the same principle of controlling the negative-sequence components, the authors in [38–40] proposed the use of resonant controllers for the positive synchronous reference frame instead of decentralizing the control system into two loops associated with

the positive- and negative-sequence components. This method relies on the strategy used to mitigate harmonics in VSCs as described in [41].

The structure of the PI resonant control (PIRC) is similar to the classical control presented in Figures 2 and 3. The classical PI controller used in the current loops are replaced with a PI plus resonant (PI + R) controller tuned at the twice the grid frequency, that is, the frequency of the negative-sequence component in the positive synchronous reference frame, resulting in the following transfer function:

$$G(s) = K_p + \frac{K_i}{s} + \frac{sK_r}{s^2 + (2\omega_s)^2} \quad (9)$$

where  $K_p$  is the proportional gain;  $K_i$  is the integral gain; and  $K_r$  is the resonant gain. In order to define the resonant gain  $K_r$  it is necessary to analyze the controller frequency response as stated in [36]. The discretization method is an important issue to be considered when designing the resonant controller for digital implementation purposes. Depending on the chosen method, the resonance peak can be attenuated and the frequency can be shifted. Tustin's method was used in this work since this is a simple and effective approach.

### 3. Assessment of DFIGs during Voltage Sags

#### 3.1. Balanced Voltage Sags

To carry out the theoretical analysis involving the influence of momentary voltage sags (MVSs) in DFIGs, the dynamic models of the induction machine are used, which are represented by Equations (1)–(4) as based on [42].

In this subsection, balanced three-phase sags are discussed, since they are the simplest phenomena that correspond to a particular case of unbalanced sags. It is assumed that the stator voltage drops instantly from its initial rated peak value  $V_s$  to a value  $V_2$  at instant  $t = t_0$ :

$$\vec{v}_s = \begin{cases} V_s e^{j\omega_s t} = V_1 e^{j\omega_s t}, & t < t_0 \\ V_2 e^{j\omega_s t}, & t \geq t_0 \end{cases} \quad (10)$$

where  $\omega_s$  is the stator angular frequency

In DFIGs, the currents are controlled by manipulating the voltages imposed on the rotor through the RSC. Thus, the variable of interest for the control system is the rotor voltage, which can be obtained from Equations (2)–(4) as [42]:

$$\vec{v}_r = \frac{L_m}{L_s} \left( \frac{d}{dt} - j\omega \right) \vec{\psi}_s + \left[ R_r + \sigma L_r \left( \frac{d}{dt} - j\omega \right) \right] \vec{i}_r \quad (11)$$

Equation (11) represents the voltage synthesized by the RSC during the normal operation. The first term of (11) is the rotor voltage portion due to the stator flux, i.e., the induced voltage in the rotor, whereas the second one is the portion due to the voltage drop caused by the rotor impedances.

The dynamic behavior of the stator flux expressed in terms of Equation (1) depends on the stator voltage, i.e., the grid voltage and the current that flows through the stator. Neglecting the voltage drop in the stator resistance, which is generally small, the stator flux in steady state can be expressed as [42]:

$$\vec{\psi}_s = \frac{V_s e^{j\omega_s t}}{j\omega_s} \quad (12)$$

Substituting (12) in (11) gives the rotor voltage in normal operation, that is:

$$\vec{v}_r = \vec{v}_s \frac{L_m}{L_s} s + \left[ R_r + \sigma L_r \left( \frac{d}{dt} - j\omega \right) \right] \vec{i}_r \quad (13)$$

where  $s$  is the machine slip. From Equation (13), it is possible to verify that generally, for a large generator, the second term is relatively smaller than the first one because the rotor

resistance and the transient inductance ( $\sigma L_r$ ) are often small. Thus, the voltage induced on the rotor depends almost exclusively on the stator flux, which in turn depends on the stator voltage described by Equation (12).

Since the term associated with the rotor voltage drop is relatively small, a first approximation analyzes the behavior of the machine during an MVS considering an open-circuit rotor, i.e.,  $\vec{i}_r = 0$ . Therefore, the goal is to analyze the behavior of the voltage induced on the rotor. Considering  $\vec{i}_r = 0$ , Equations (1) and (2) lead to:

$$\frac{d\vec{\psi}_s}{dt} = \vec{v}_s - \frac{R_s}{L_s} \vec{\psi}_s \quad (14)$$

Before the dip at  $t < t_0$ , the stator flux in steady state is totally produced by the voltage on the stator, i.e., there is only the presence of the forced system response. Thus, Equation (12) becomes:

$$\vec{\psi}_{sf1} = \frac{V_1 e^{j\omega_s t}}{j\omega_s} \quad (15)$$

This flux component is used as an initial condition for solving Equation (14) aiming to calculate the flux at the moment when the voltage sag occurs. Assuming that the phenomenon starts at  $t_0 = 0$ , i.e., at the beginning of the sag the voltage is at the value maximum (worst-case condition), the stator flux response is given by [42]:

$$\vec{\psi}_s = \frac{V_2}{j\omega_s} e^{j\omega_s t} + \frac{(V_1 - V_2)}{j\omega_s} e^{-\frac{t}{\tau_s}} = \vec{\psi}_{sf2} + \vec{\psi}_{sn} \quad (16)$$

where  $\tau_s = \frac{L_s}{R_s}$  is the stator time constant;  $\vec{\psi}_{sf2}$  is the forced response due to the remaining voltage during the sag; and  $\vec{\psi}_{sn}$  is the natural flux that induced the stator voltage transient. It is observed that the first term is constant and rotates with the synchronous frequency in the complex plane, while the second one is a fixed vector, whose amplitude decays with the stator time constant.

According to Equation (11), one can see that the two flux components induce voltage components on the rotor. From Equation (13) and considering  $i_r = 0$ , the induced voltage on the rotor caused by the forced flux yields [42]:

$$\vec{v}_{ra}^r = \vec{v}_{rf}^r + \vec{v}_{rn}^r = \frac{L_m}{L_s} \left( V_2 s e^{j\omega_r t} - \left( \frac{1}{\tau_s} + j\omega \right) \frac{V_1 - V_2}{j\omega_s} e^{-\frac{t}{\tau_s}} e^{-j\omega t} \right) \quad (17)$$

Analyzing Equation (17), it is observed that the first term has an amplitude and a frequency considerably lower than those of the second term. This is because the slip is low within the operation range of the DFIG. The second term has a frequency equal to the rotor electric frequency.

The worst case, i.e., when the voltage reaches the maximum value, occurs when the remaining voltage ( $V_2$ ) is zero and the rotating speed is as high as possible. The rotor voltage reaches its highest value when the sag occurs and the stator voltage reaches a maximum value. In this sense, the maximum voltage appears exactly at the beginning of the dip. If the voltage on the stator is zero when the sag occurs, the maximum induced voltage will appear one-fourth cycle after the initial instant. If the stator time constant is high, the maximum voltage will be nearly the same in both cases. Otherwise, the second case will present a lower maximum voltage.

A more in-depth analysis of the DFIG behavior during balanced voltage sags can be found in [23,36], whereas the following statements are valid for balanced voltage sags:

- During balanced sags, the main problem is the natural flux component, which induces a high voltage on the rotor, causing high oscillatory currents that may damage the converter;

- The natural component produces oscillations with the same frequency as that of the stator, which are reflected in the torque pulsations. This behavior is undesired from the point of view of the mechanical coupling between the generator and turbine;
- The natural component of the stator currents causes power oscillations in the injected active and reactive powers, which are undesired from the point of view of the power system.

### 3.2. Unbalanced Voltage Sags

The classical equations of the induction machine corresponding to (1)–(4) will be used in the theoretical analysis of unbalanced MVSSs. Equations (11)–(14) as derived in the previous subsection will also be useful in the mathematical analysis of unbalanced sags in DFIGs. This study is based on the benchmarks given in [43].

While in a balanced three-phase system there are only positive-sequence components, negative-sequence components also appear during unbalanced sags. The classical equations of the induction machine represented in the synchronous reference frame can be divided into positive- and negative-sequences terms as follows [44]:

$$\vec{v}_{s\pm} = R_s \vec{i}_{s\pm} + \frac{d\vec{\psi}_{s\pm}}{dt} \pm j\omega_s \vec{\psi}_{s\pm} \quad (18)$$

$$\vec{v}_{r\pm} = R_r \vec{i}_{r\pm} + \frac{d\vec{\psi}_{r\pm}}{dt} \pm j\omega_r \vec{\psi}_{r\pm} \quad (19)$$

$$\vec{\psi}_{s\pm} = L_s \vec{i}_{s\pm} + L_m \vec{i}_{r\pm} \quad (20)$$

$$\vec{\psi}_{r\pm} = L_r \vec{i}_{r\pm} + L_m \vec{i}_{s\pm} \quad (21)$$

The differential equations of the positive- and negative-sequence components are represented together aiming to obtain a more compact expression. The variables can be decomposed into  $dq$  components and expressed in terms of the positive and negative sequences in different referential frames, resulting in [45]:

$$A^+_{dq} = A^+_{dq+} + A^+_{dq-} = A^+_{dq+} + A^-_{dq-} e^{j2\omega_s t} \quad (22)$$

The superscript  $dq$  stands for the synchronous, whereas “+” and “−” denote the positive- and negative-sequence terms, respectively.

Comparing (22) with (18) to (21) and applying the Laplace transform, it is possible to manipulate the equations and obtain the stator flux linkage as a function of the stator voltage and rotor current [36]:

$$\psi^{\pm}_{sd\pm}(s) = \frac{(s + 1/\tau_s) V^{\pm}_{sd\pm}(s) + L_m/\tau_s (s + 1/\tau_s) I^{\pm}_{rd\pm}(s)}{(s^2 + 2\frac{1}{\tau_s} s + \omega_s^2)} \quad (23)$$

$$\psi^{\pm}_{sq\pm}(s) = \frac{\mp \omega_s V^{\pm}_{sd\pm}(s) + L_m/\tau_s (s + 1/\tau_s) I^{\pm}_{rq\pm}(s)}{(s^2 + 2\frac{1}{\tau_s} s + \omega_s^2)} \quad (24)$$

As previously mentioned, the stator flux linkage induces voltages on the rotor circuit. A good approximation for obtaining the induced rotor voltage lies in using the open-rotor analysis [46], i.e., neglecting the voltage drop on the rotor impedance since it is generally small. From Equations (19)–(24) and considering that the rotor currents are null, the rotor voltages can be calculated in the frequency domain as [36]:

$$V_{rd}^+ = \frac{L_m}{L_s} \left( \frac{s^2 + \frac{1}{\tau_s} s \pm \omega_r \omega_s}{s^2 + 2\frac{1}{\tau_s} s + \omega_s^2} \right) (V_{sd+}^+ + e^{-j2\omega_s t} V_{sd-}^-) \quad (25)$$

$$V_{r_q}^+ = \frac{L_m}{L_s} \left( \frac{(\omega_{r\pm} \mp \omega_s)s \pm \omega_{r\pm}/\tau_s}{s^2 + 2\frac{1}{\tau_s}s + \omega_s} \right) (V_{s_{d+}}^+ + e^{-j2\omega_s t} V_{s_{d-}}^-) \quad (26)$$

Equations (25) and (26) show that the induced rotor voltage depends on the positive- and negative-sequence components of the  $d$  axis stator voltage. In the synchronous reference frame, the positive-sequence term induces a constant component on the rotor voltage, whereas the negative-sequence term leads to an oscillatory component at  $2\omega_s$ . If the voltage imbalance is considerable, the negative-sequence component of the rotor voltage is much higher than the positive-sequence one. Depending on the control action, this voltage may cause high rotor currents and damage the converter.

A more in-depth analysis of the DFIG behavior submitted to unbalanced sags can be found in [36], whereas the main statements for unbalanced voltage sags are:

- During unbalanced sags, the negative-sequence component of the rotor voltage is the main cause of excessive rotor overcurrents.
- While the natural flux component decays, the negative sequence is present during all the sags with its amplitude dependent only on the unbalance.
- In the unbalanced case, the problem is even worse when there is also the presence of the natural component, since the overcurrents are caused by the sum of natural- and negative-sequence components.
- Electromagnetic torque and grid powers will oscillate with twice the grid frequency and higher amplitudes due to the natural- and negative-sequence components.

#### 4. Thermal Modeling

The WECS described in Section 2 was implemented and analyzed using PLECS software and considering the specifications given in Table 1.

**Table 1.** Specifications of the simulated system [36].

Parameter	Value
GSC voltage	380 V
Grid frequency	60 Hz
Rated output power	2.0 MW
DC-link voltage	698 V
Switching frequency	3 kHz
Stator voltage	690 V
Stator current	1414.20 A
Stator resistance	0.002381 $\Omega$
Stator leakage inductance	0.07579 mH
Rotor voltage	1380 V
Rotor current	707.10 A
Rotor resistance	0.002381 $\Omega$
Rotor leakage inductance	0.060481 mH
Magnetizing inductance	0.0023 H
Stator/rotor turns ratio	0.5
Inertia moment	59.47 kg/m <sup>2</sup>
Friction coefficient	0.007 N·m·s
Number of pole pairs	2

Since many manufacturers recommend a module capable of supporting a voltage around 60% of the DC-link voltage, IGBT power modules rated at a blocking voltage of 1200 V were chosen. The module should also support the maximum current produced in the machine rotor. Therefore, module FF1500R12IE5 by Infineon, whose ratings are given in [47], was used in the tests.

This module has a current capacity higher than the rated current of the machine rotor. Therefore, in theory, using a single module per phase would be enough for ensuring the safe operation under normal conditions. However, the system was scaled up considering

two modules arranged in parallel so that it can operate properly even when subjected to severe voltage sags. This association also aims to avoid the overheating of IGBTs and body diodes. Although the GSC has a lower maximum current than the RSC, the same module designed for the RSC is employed in the analysis. Considering that the GSC is far less sensitive to disturbances caused by voltage sags, a preliminary analysis carried out by the authors showed that there is no need for paralleling the modules to ensure the safe operation under both normal and sag conditions.

Using data obtained from the semiconductor datasheet, software PLECS is capable of generating the very same characteristic curves provided by manufacturers as shown in Figures 4 and 5.

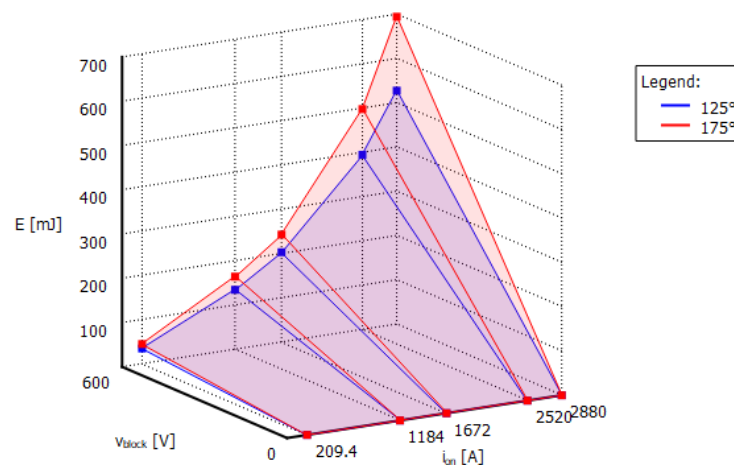


Figure 4. Turn-on losses represented in PLECS thermal library.

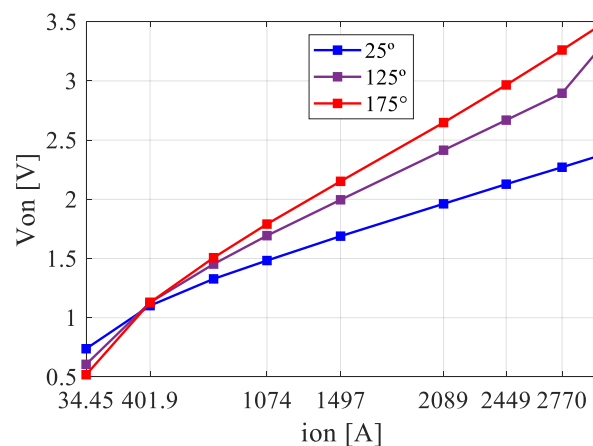


Figure 5. Characteristic curves generated in PLECS thermal library.

Power semiconductor manufacturers usually assess the thermal impedance inside the power module, whereas the values are provided in terms of a multi-layer Foster structure as listed in Table 2.

Table 2. Junction-to-case thermal impedance of power module FF1500R12IE5.

Component	Parameter	1st	2nd	3rd	4th
IGBT	$R$ (K/kW)	0.527	8.61	8.74	1.63
	$\tau$ (s)	0.0012	0.0271	0.0739	0.967
Diode	$R$ (K/kW)	2.72	13.4	16.5	2.35
	$\tau$ (s)	0.0012	0.0221	0.0782	1.53



Based on the semiconductor parameters, as well as using calculations and linear interpolations, the software can calculate the power losses and thus estimate the junction temperatures of semiconductor devices.

In this work, a commercial heatsink that supports two modules well spaced from each other was considered for obtaining a more uniform thermal distribution. After an extensive search carried out by the authors, model P16/300 by SEMIKRON was adopted [48]. Thus, considering a heatsink of 300 mm with two IGBT modules, a thermal resistance of 0.0024 K/W was determined from the simulation tests. It is worth mentioning that the heatsink thermal capacitance was neglected, since the thermal loading of interest is the one of the power semiconductors.

## 5. Results and Discussion

### 5.1. Balanced Voltage Sags

In order to understand the behavior of the DFIG-based WECS during voltage sags, the system specified in Table 1 was analyzed in PLECS environment. The provided analysis refers always to the beginning of the dip, since this moment is generally the worst-case condition. In the first test, the system was submitted to a balanced three-phase voltage sag of 20%, whereas the generator operates at the supersynchronous speed (2340 rpm) and rated power (2.0 MW).

The stator and rotor currents are presented in Figure 6a,b, respectively. The variables of main interest are the rotor currents, because the voltages induced on the rotor cause overcurrents that may damage the converter. When the sag occurs, it is observed that the rotor current peak reaches almost four times the current under normal conditions. This peak is due to the voltage induced by the natural flux at the moment of the transient. Analyzing the waveforms, two components can be easily identified: a low-frequency component due to the forced rotor voltage that remains throughout the dip and a higher frequency component due to the voltage induced by the natural flux. It is observed that this latter portion remains for the nearly the whole sag, while decaying its amplitude.

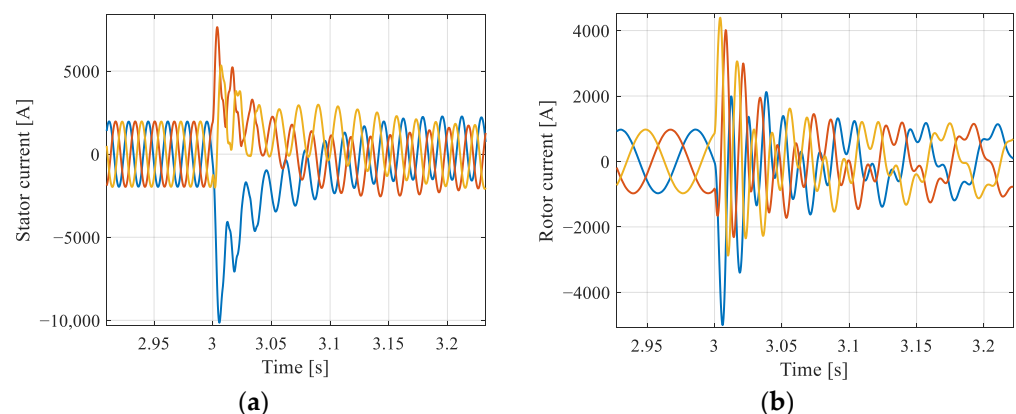


**Figure 6.** Currents during a balanced voltage sag: (a) stator currents and (b) rotor currents.

The natural component is also reflected in the powers flowing through the different circuits as shown in Figure 7. The oscillation in the power generated by the system is undesired, as it degrades the grid power quality. The measured quantities are negative, denoting the power injection into the grid. During the sag, the powers decrease as a consequence of the grid voltage reduction and the average current limitation imposed by the power converter.

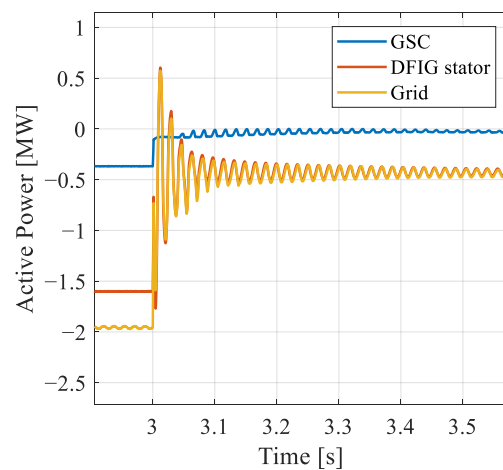


**Figure 7.** Active powers during a balanced voltage sag.

The rotor current oscillations also reflect on the GSC currents and DC-link voltage. From Figure 8, one can see that at the beginning of the sag the DC-link voltage tends to increase because of the high rotor currents flowing to the capacitors. Therefore, the GSC direct current (active power) increases in Figure 9 to keep the DC-link voltage constant. Nevertheless, owing to the converter current limitation and the fast transient, the DC-link voltage tends to increase and, in order to avoid damaging the converter, a brake chopper is used to limit the DC-link voltage at a maximum value of 733 V.

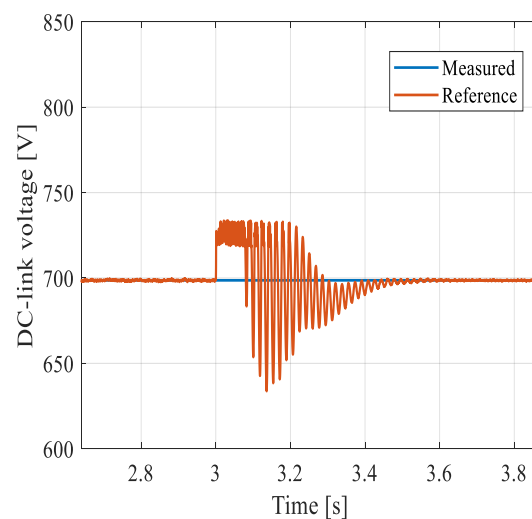


**Figure 8.** DC-link voltage during a balanced voltage sag.

Figure 10 shows the  $d$  and  $q$  axis components of the currents in the RSC, which suddenly increase at the beginning of the dip due to the natural component in the rotor voltage. The natural component occurs in the form of a 60 Hz oscillation in the synchronous reference frame. However, the reference signal remains at the maximum value established by the RSC control loops, (1500 A). In turn, the transient due to the natural component causes the currents to reach values much higher than the rated value.

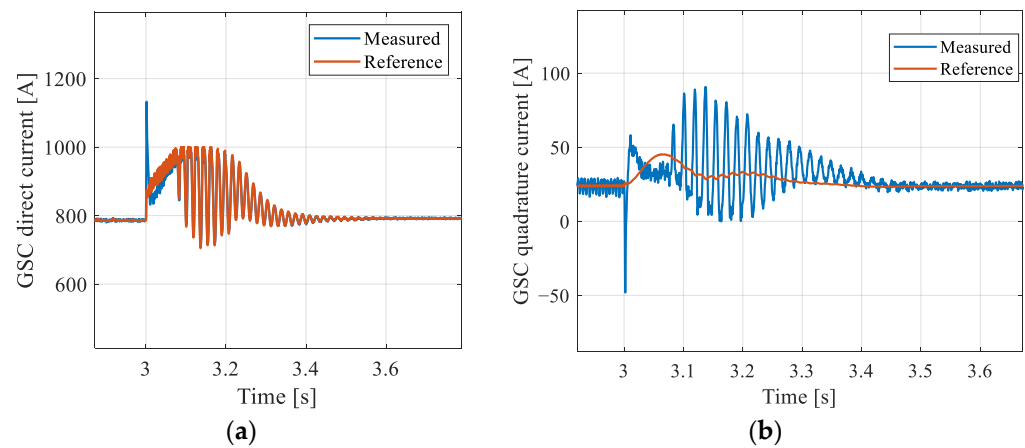


**Figure 9.** GSC currents: (a)  $d$  axis component and (b)  $q$  axis component.

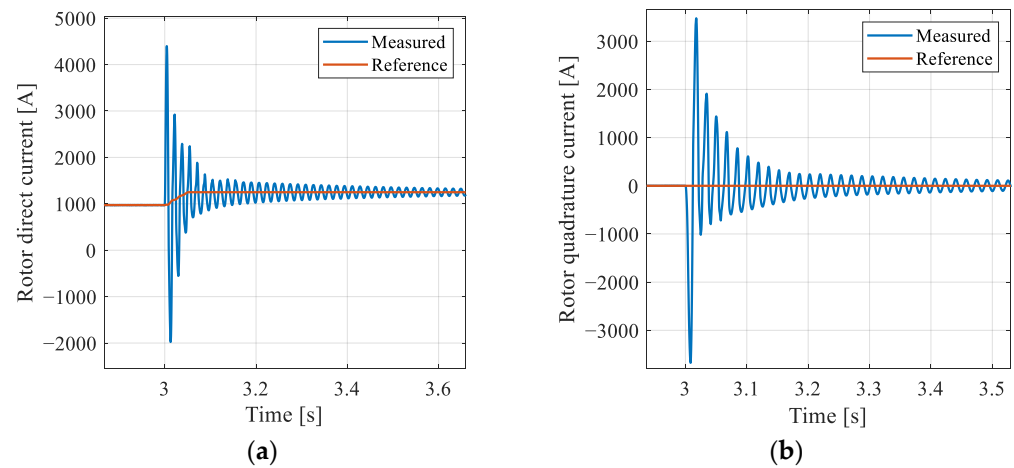


**Figure 10.** RSC currents during a balanced voltage sag: (a)  $d$  axis component and (b)  $q$  axis component.

Since semiconductors are subject to high currents and voltage transients during voltage sags, an analysis of the junction temperature behavior is quite important. Figure 11a,b show the junction temperatures in the modules used in the GSC and RSC. It is possible to notice the harmful effects associated with the oscillations, which are caused by the voltage sag and reflect on the operating temperatures of power modules.

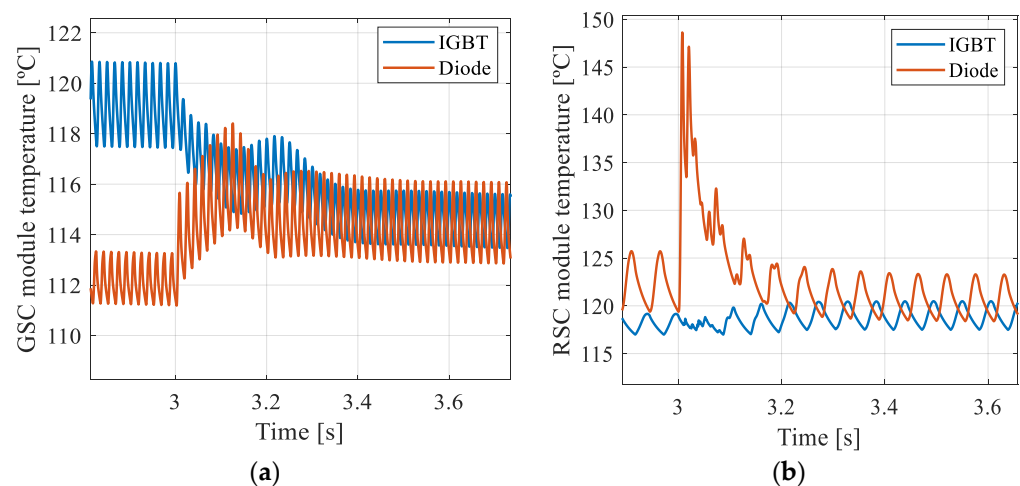


**Figure 11.** Junction temperature of the power module during a balanced voltage sag: (a) GSC and (b) RSC.

The behavior of the power modules used in GSC and RSC are slightly different under normal operating conditions. The thermal stress is higher for the IGBTs and body diodes in the GSC and RSC, respectively. This is because the power flows from the AC side to the DC one in the RSC, whereas the power flow direction is opposite in the GSC. In particular, Figure 11a shows that there is an increase in the diode junction temperature at the beginning of the sag, caused by the spikes that occur in both the DC-link voltage and GSC currents.

It is worth noting that the RSC is the most affected element, since the natural component causes overcurrents in the rotor, resulting in spikes in the junction temperature of the semiconductor devices according to Figure 11b. It is also observed that the thermal cycling for the components of the power modules in the RSC is lower than for that in the GSC. In other words, the devices are exposed to higher temperatures for a longer time. This is because the currents in the RSC have a lower frequency (approximately 18 Hz) than that of the GSC (60 Hz).

It is important to highlight that the junction temperatures of the semiconductor devices did not exceed the limit that power module supports, that is, a maximum of 175 °C. Therefore, the thermal design ensures the safe operation of the system, even when subjected to severe balanced voltage sags. This is a consequence of the design conditions adopted in this study, thus evidencing that it is necessary to increase the current capacity of the power converter to meet grid code requirements.

### 5.2. Unbalanced Voltage Sags

In this section, the behavior of the WECS when submitted to an unbalanced voltage sag of 20% is assessed in terms of relevant variables. The instant at which the phenomenon occurs was defined in such a way that the highest natural component is induced. This test was performed at supersynchronous speed (2340 rpm) and rated power (2.0 MW).

The stator and rotor currents are presented in Figure 12a,b, respectively. In addition to the natural component, there is the presence of the negative-sequence component, which causes oscillations at a frequency equal to twice the stator frequency (120 Hz). Similarly to the balanced case, it is possible to observe the presence of high current peaks caused by the natural component in the stator and rotor, reaching almost five times the rated value. However, compared with the balanced case, the peak caused by the natural component in either condition is not so different. In turn, the current values during the sag are higher for the unbalanced condition, since there is the influence of the negative-sequence component.

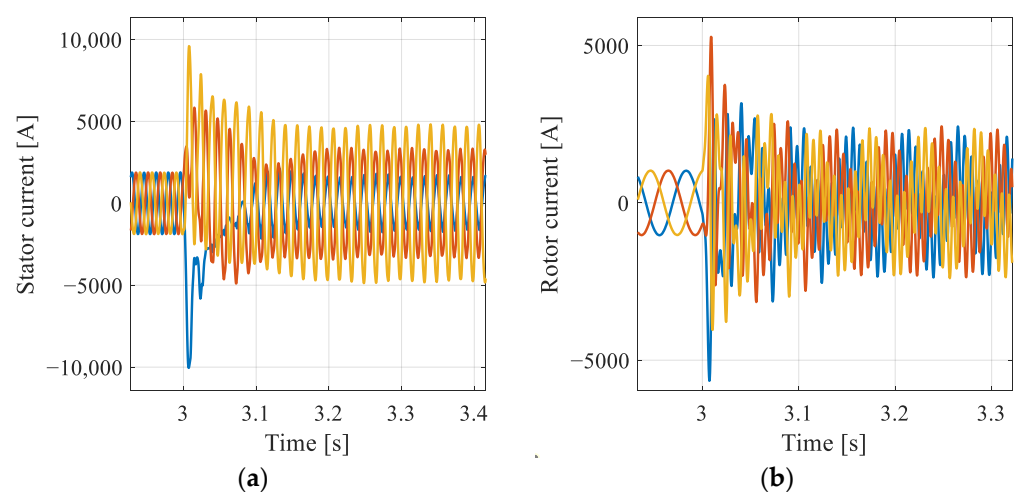


**Figure 12.** DFIG currents for an unbalanced voltage sag of 20%: (a) stator currents and (b) rotor currents.

The negative-sequence component also causes oscillations in the stator power as seen in Figure 13. Such oscillations are undesirable and may further contribute to the degradation

of the grid power quality. The GSC currents and the DC-link voltage represented in Figures 14 and 15, respectively, are also affected by the negative-sequence terms.

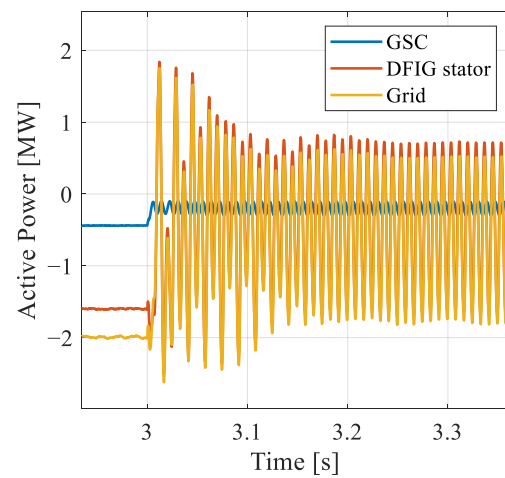


**Figure 13.** Active powers for an unbalanced voltage sag of 20%.

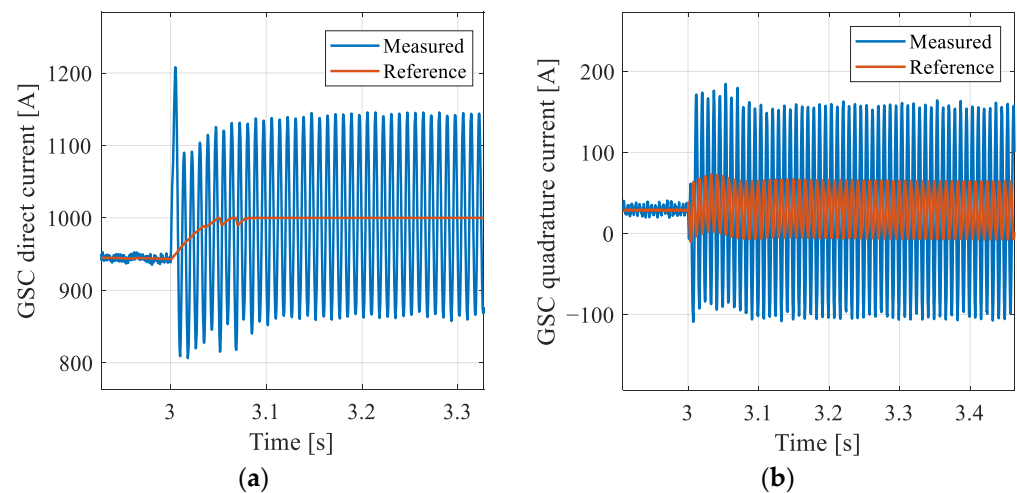


**Figure 14.** GSC currents for an unbalanced voltage sag of 20%: (a)  $d$  axis component and (b)  $q$  axis component.

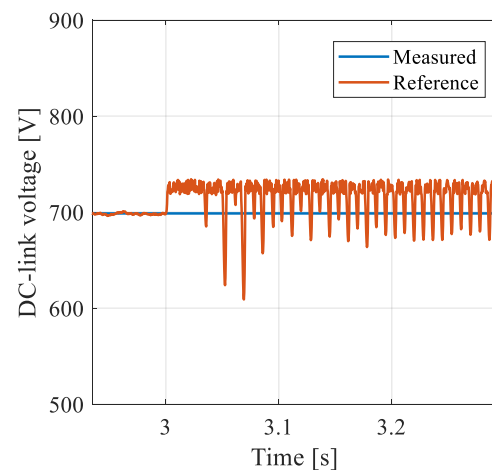


**Figure 15.** DC-link voltage for an unbalanced voltage sag of 20%.

From the rotor currents in the synchronous reference shown in Figure 16, it is possible to provide a more comprehensive analysis of the control system performance. It is observed that the natural component decays and only the negative-sequence component remains throughout the dip. This is because the controller saturates as a consequence of the severity of the sag, demanding a higher voltage as shown in Figure 17. Analyzing the rotor voltage in Figure 17, it becomes evident that the peak values of the rotor voltages at the beginning of the sag do exceed the converter limit (400 V). Under this condition, the RSC operates in the overmodulation region. In this particular case, the resonant controller cannot ensure the accurate control of the rotor currents.

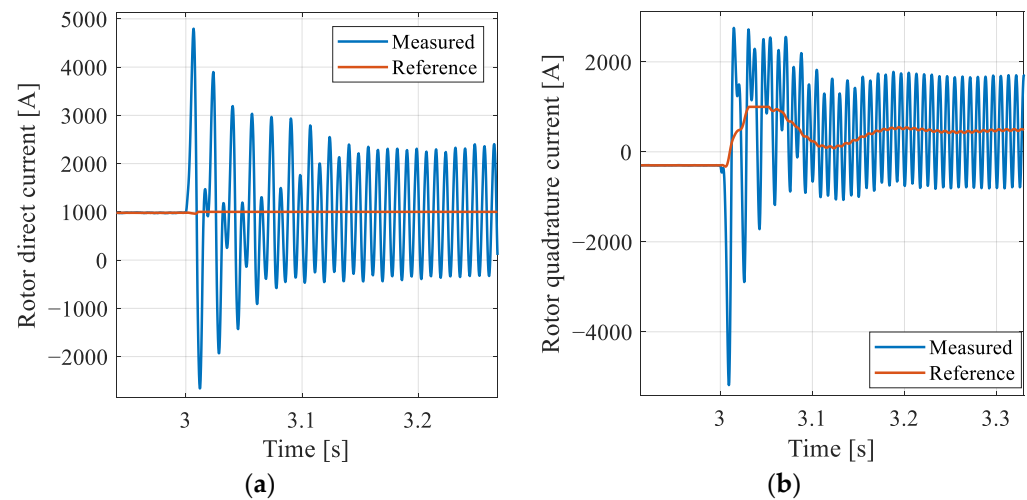


**Figure 16.** RSC currents for an unbalanced voltage sag of 20%: (a)  $d$  axis component and (b)  $q$  axis component.

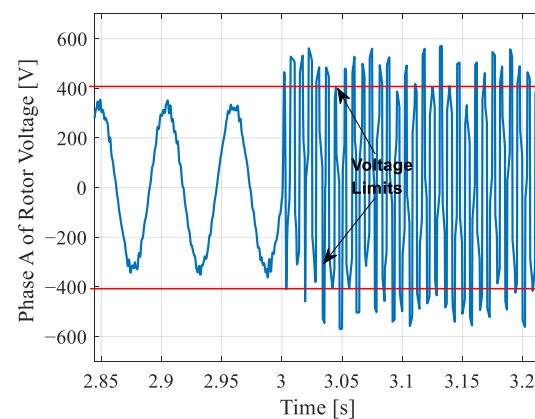


**Figure 17.** Rotor voltage in phase A for an unbalanced voltage sag of 20%.

The semiconductor devices are also subjected to oscillations caused by the negative-sequence component. Figure 18a shows the semiconductor temperatures in the GSC. At the beginning of the dip, there is a sudden increase in the diode temperature. Similar to the case of the balanced sags, this is due to the increase in the GSC currents in an attempt to keep the output power constant. The increase in the diode temperature is directly related to the increase in the GSC currents. The negative-sequence component remains throughout the dip, as the controller saturates owing to the restriction imposed by the converter voltage limits. Although the IGBT temperature was expected to decrease at the beginning of the sag, similar to the balanced case, it remains almost unchanged during the entire phenomenon. This is because the controller is ineffective in dampening the negative-sequence component that contributes to the increase in GSC currents.



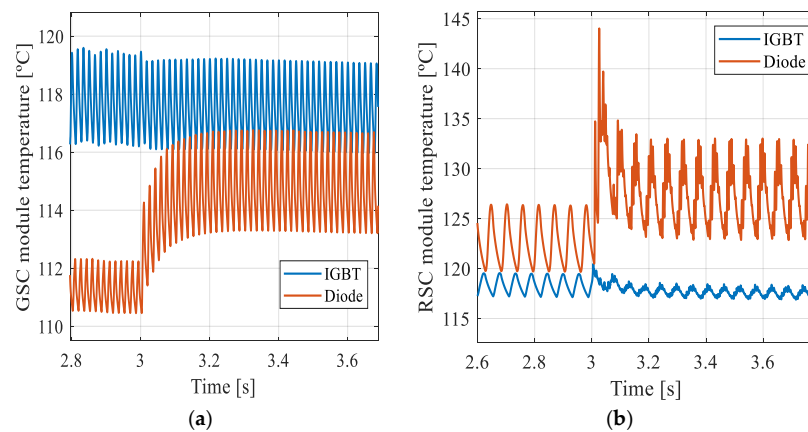


**Figure 18.** Junction temperature of the power module for an unbalanced sag of 20%: (a) GSC module and (b) RSC module.

Figure 18b presents the temperature of the semiconductors used in the RSC. One can observe the peak in the diode temperature caused by the natural component as in balanced sags. Moreover, the negative-sequence component is responsible for keeping the temperature high even after the natural component decays. It is reasonable to state that the diode is the most affected component, since the power flows from the AC to the DC side in the RSC.

In order to enhance the voltage margin for the resonant controller, the DC-link voltage was increased to approximately 1000 V. As previously mentioned, manufacturers do recommend a module capable of supporting a voltage around 60% of the DC-link voltage. Therefore, it was necessary to replace the former power module with model FF1500R17IP5P [49], which is rated at 1700 V. This test was also performed at the supersynchronous speed (2340 rpm), rated power (2.0 MW) condition, and phase-to-phase voltage sag of 70%. Only the variables that best evidence the performance of the resonant controller will be analyzed in this test.

In this sense, Figure 19 shows the GSC currents, whereas the action of the resonant controller can be observed. The rotor currents in the synchronous reference frame represented in Figure 20 also allow the evaluation of the control system performance. In this case, the resonant controller is capable of regulating the negative-sequence components and the transient behavior of the natural component can be observed. Once the DC-link voltage is higher, it provides the system with a broader control margin as observed in Figure 21. Figure 21 clearly evidences that, despite the occurrence of a more severe sag, the converter is capable of operating within the limits so as to avoid overmodulation.

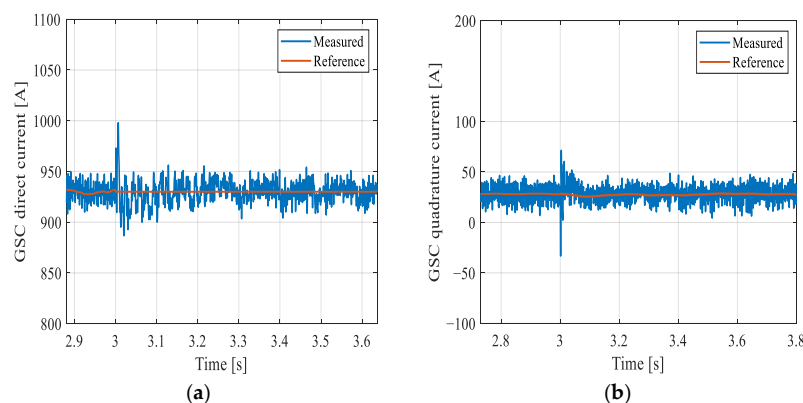


**Figure 19.** GSC currents during an unbalanced voltage sag of 70%: (a)  $d$  axis component and (b)  $q$  axis component.

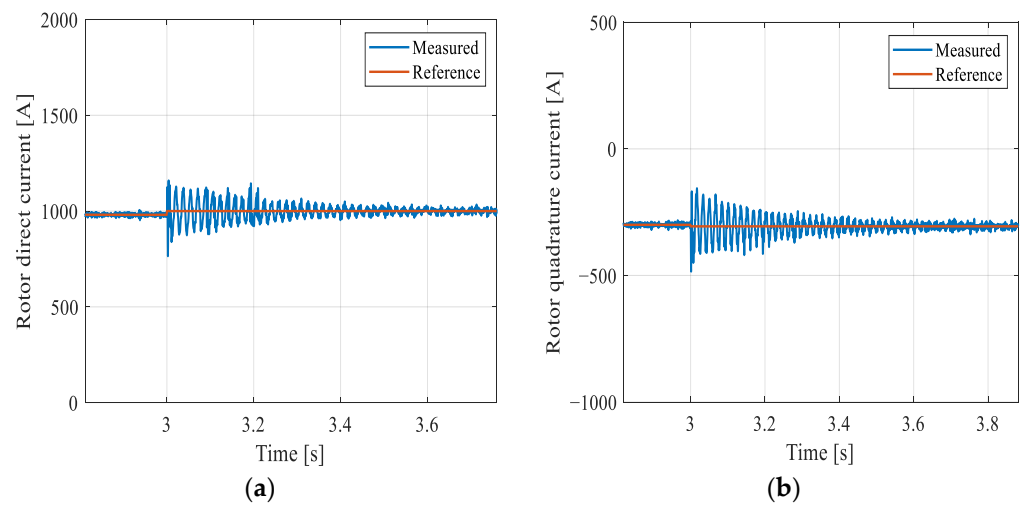


**Figure 20.** Rotor currents during an unbalanced voltage sag of 70%: (a)  $d$  axis component and (b)  $q$  axis component.

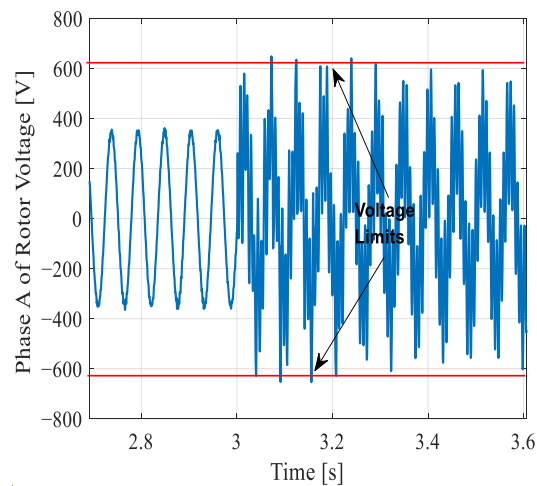


**Figure 21.** Rotor voltages in phase A during an unbalanced voltage sag of 70%.

Figure 22a shows the temperature of the power semiconductor module used in the GSC. At the beginning of the sag, there is a small increase in the diode temperature. This is because the DC-link voltage tends to increase, causing the GSC currents to increase as a consequence in order to keep both the voltage and power constant. Figure 22b represents the temperatures in the semiconductors of the RSC. The average temperature of the devices is slightly lower due to the severity of the sage, although a further reduction in this quantity was expected. However, it does not occur because the higher voltage thresholds required by the control action as associated with the power converter operation do lead to higher operating temperatures, especially in the diode. Another possible cause is that the negative-sequence component may remain during the whole dip. Since the thermal dynamics is slower than that of the currents, the system may still remain under the harmful effects of the negative-sequence component.

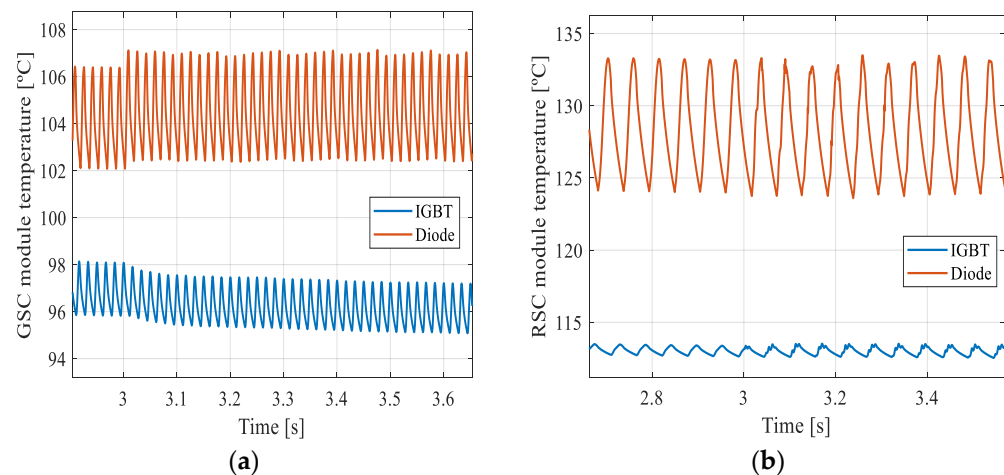


**Figure 22.** Junction temperature of the power module during an unbalanced voltage sag of 70%: (a) GSC and (b) RSC.

## 6. Conclusions

This work has presented a comprehensive thermal analysis of a DFIG-based WECS. The junction temperatures of power semiconductors were evaluated in order to verify the thermal stress to which they are subjected. The results showed the behavior of the most relevant variables when voltage sags occur. The analysis clearly evidences that the DFIG is very sensitive to such power quality phenomena, considering that the oscillations in the stator flux cause overcurrents in the rotor due to the presence of natural- and negative-sequence components. This issue becomes more intense as the sag level increases, since the higher the value assumed by the aforementioned components, the higher the influence on the increase in the junction temperature of semiconductors. Therefore, it is reasonable to state that the thermal profile of power semiconductors is of major importance for designing the system while ensuring its safe operation during such phenomena.

The PI + R controller adopted in the study proved to be quite effective in reducing the negative-sequence component, which is not high during the sag so as to avoid the excessive increase in the operating temperature of power semiconductors. In turn, other studies have shown that this strategy may become more effective if the voltage capability of the converter is increased, thus providing the control system with a wider margin. Thus, it is necessary to choose IGBTs rated at higher voltages, thus increasing the overall cost.

Future work includes the analysis of LVRT strategies from the point of view of thermal stresses on semiconductors. This analysis aims to determine the best solutions for protecting the DFIG under such severe conditions. The whole study is supposed to be validated using a laboratory setup comprising a small-scale WECS.

**Author Contributions:** Conceptualization, V.F.M.; methodology, V.F.M.; validation, I.R.d.O.; formal analysis, I.R.d.O.; investigation, I.R.d.O.; writing—original draft preparation, I.R.d.O.; writing—review and editing, F.L.T. and V.F.M.; supervision, F.L.T. and V.F.M. All authors have read and agreed to the published version of the manuscript.

**Funding:** This research was funded by the Coordenação de Aperfeiçoamento de Pessoal de Nível Superior—Brazil (CAPES)—Finance Code 001. The authors would also like to acknowledge Conselho Nacional de Desenvolvimento Científico e Tecnológico (CNPq)—Project 436213/2018-4; Fundação de Amparo à Pesquisa do Estado de Minas Gerais (FAPEMIG)—Project APQ-01187-18; and Instituto Nacional de Ciência e Tecnologia em Energia Elétrica (INERGE) for supporting this work.

**Institutional Review Board Statement:** Not applicable.

**Informed Consent Statement:** Not applicable.

**Data Availability Statement:** Data available on request from the authors.

**Conflicts of Interest:** The authors declare no conflict of interest.

## References

- Global Wind Energy Council. *Global Wind Report 2021*; Global Wind Energy Council: Brussels, Belgium, 2021.
- Shen, Y.; Zhang, B.; Liang, L.; Cui, T. A novel control strategy for enhancing the LVRT and voltage support capabilities of DFIG. In *IOP Conference Series: Earth and Environmental Science*; IOP Publishing: Bristol, UK, 2018; Volume 121, p. 042035.
- Saeed, M.A.; Khan, H.M.; Ashraf, A.; Qureshi, S.A. Analyzing effectiveness of LVRT techniques for DFIG wind turbine system and implementation of hybrid combination with control schemes. *Renew. Sustain. Energy Rev.* **2018**, *81*, 2487–2501. [\[CrossRef\]](#)
- Xiang, D.; Ran, L.; Tavner, P.J.; Yang, S. Control of a doubly fed induction generator in a wind turbine during grid fault ride-through. *IEEE Trans. Energy Convers.* **2006**, *21*, 652–662. [\[CrossRef\]](#)
- Yang, L.; Xu, Z.; Ostergaard, J.; Dong, Z.Y.; Wong, K.P. Advanced control strategy of DFIG wind turbines for power system fault ride through. *IEEE Trans. Power Syst.* **2011**, *27*, 713–722. [\[CrossRef\]](#)
- ONS. *Procedimentos de Rede—Submódulo 3.6: Requisitos Técnicos Mínimos Para a Conexão à Rede Básica*; ONS: Rio de Janeiro, Brazil, 2009.
- Justo, J.; Bansal, R. Parallel R-L configuration crowbar with series R-L circuit protection for LVRT strategy of DFIG under transient-state. *Electr. Power Syst. Res.* **2018**, *154*, 299–310. [\[CrossRef\]](#)
- Naderi, S.B.; Negnevitsky, M.; Muttaqi, K.M. A modified DC chopper for limiting the fault current and controlling the DC-link voltage to enhance fault ride-through capability of doubly-fed induction-generator-based wind turbine. *IEEE Trans. Ind. Appl.* **2018**, *55*, 2021–2032. [\[CrossRef\]](#)
- Gray, C.; Buque, C.; Chowdhury, S. AC series dynamic resistor protection scheme with switching control for doubly fed induction generator based WECS. In Proceedings of the 2016 IEEE Power and Energy Society General Meeting (PESGM), Boston, MA, USA, 17–21 July 2016; pp. 1–5.
- Kim, J.; Muljadi, E.; Gevorgian, V.; Hoke, A.F. Dynamic capabilities of an energy storage-embedded DFIG system. *IEEE Trans. Ind. Appl.* **2019**, *55*, 4124–4134. [\[CrossRef\]](#)
- Huang, J.; Zhang, L.; Sang, S.; Xue, X.; Zhang, X.; Sun, T.; Wu, W.; Gao, N. Optimized series dynamic braking resistor for LVRT of doubly-fed induction generator with uncertain fault scenarios. *IEEE Access* **2022**, *10*, 22533–22546. [\[CrossRef\]](#)
- Liang, J.; Qiao, W.; Harley, R.G. Feed-forward transient current control for low-voltage ride-through enhancement of DFIG wind turbines. *IEEE Trans. Energy Convers.* **2010**, *25*, 836–843. [\[CrossRef\]](#)
- Zhu, D.; Zou, X.; Deng, L.; Huang, Q.; Zhou, S.; Kang, Y. Inductance-emulating control for DFIG-based wind turbine to ride-through grid faults. *IEEE Trans. Power Electron.* **2016**, *32*, 8514–8525. [\[CrossRef\]](#)
- Zhu, D.; Zou, X.; Zhou, S.; Dong, W.; Kang, Y.; Hu, J. Feedforward current references control for DFIG-based wind turbine to improve transient control performance during grid faults. *IEEE Trans. Energy Convers.* **2017**, *33*, 670–681. [\[CrossRef\]](#)
- Liang, J.; Howard, D.F.; Restrepo, J.A.; Harley, R.G. Feedforward transient compensation control for DFIG wind turbines during both balanced and unbalanced grid disturbances. *IEEE Trans. Ind. Appl.* **2013**, *49*, 1452–1463. [\[CrossRef\]](#)
- Liu, R.; Yao, J.; Wang, X.; Sun, P.; Pei, J.; Hu, J. Dynamic stability analysis and improved LVRT schemes of DFIG-based wind turbines during a symmetrical fault in a weak grid. *IEEE Trans. Power Electron.* **2019**, *35*, 303–318. [\[CrossRef\]](#)
- Ruiz-Cruz, R.; Sanchez, E.N.; Loukianov, A.G.; Ruz-Hernandez, J.A. Real-time neural inverse optimal control for a wind generator. *IEEE Trans. Sustain. Energy* **2018**, *10*, 1172–1183. [\[CrossRef\]](#)
- Ozsoy, E.; Padmanaban, S.; Mihet-Popa, L.; Fedák, V.; Ahmad, F.; Akhtar, R.; Sabanovic, A. Control strategy for a grid-connected inverter under unbalanced network conditions—A disturbance observer-based decoupled current approach. *Energies* **2017**, *10*, 1067. [\[CrossRef\]](#)
- Kong, X.; Wang, X.; Abdelbaky, M.A.; Liu, X.; Lee, K.Y. Nonlinear MPC for DFIG-based wind power generation under unbalanced grid conditions. *Int. J. Electr. Power Energy Syst.* **2022**, *134*, 107416. [\[CrossRef\]](#)
- Xiong, L.; Li, P.; Wang, J. High-order sliding mode control of DFIG under unbalanced grid voltage conditions. *Int. J. Electr. Power Energy Syst.* **2020**, *117*, 105608. [\[CrossRef\]](#)
- Rafiee, Z.; Heydari, R.; Rafiee, M.; Aghamohammadi, M.R.; Blaabjerg, F. Enhancement of the LVRT capability for DFIG-based wind farms based on short-circuit capacity. *IEEE Syst. J.* **2022**, 1–12. [\[CrossRef\]](#)
- Hiremath, R.; Moger, T. Modified Super Twisting algorithm based sliding mode control for LVRT enhancement of DFIG driven wind system. *Energy Reports* **2022**, *8*, 3600–3613. [\[CrossRef\]](#)
- Mendes, V.F.; de Sousa, C.V.; Silva, S.; Rabelo, B.C.; Hofmann, W. Modeling and ride-through control of doubly fed induction generators during symmetrical voltage sags. *IEEE Trans. Energy Convers.* **2011**, *26*, 1161–1171. [\[CrossRef\]](#)
- Zhou, L.; Liu, J.; Zhou, S. Improved demagnetization control of a doubly-fed induction generator under balanced grid fault. *IEEE Trans. Power Electron.* **2014**, *30*, 6695–6705. [\[CrossRef\]](#)
- Blaabjerg, F.; Chen, Z.; Kjaer, S.B. Power electronics as efficient interface in dispersed power generation systems. *IEEE Trans. Power Electron.* **2004**, *19*, 1184–1194. [\[CrossRef\]](#)
- Blaabjerg, F.; Ma, K.; Zhou, D. Power electronics and reliability in renewable energy systems. In Proceedings of the 2012 IEEE International Symposium on Industrial Electronics, Hangzhou, China, 28–31 May 2012; pp. 19–30.
- Zhou, D.; Blaabjerg, F. Thermal analysis of two-level wind power converter under symmetrical grid fault. In Proceedings of the IECON 2013-39th Annual Conference of the IEEE Industrial Electronics Society, Vienna, Austria, 10–13 November 2013; pp. 1904–1909.

28. Zhou, D.; Blaabjerg, F.; Lau, M.; Tonnes, M. Thermal behavior of doubly-fed induction generator wind turbine system during balanced grid fault. In Proceedings of the 2014 IEEE Applied Power Electronics Conference and Exposition-APEC 2014, Fort Worth, TX, USA, 16–20 March 2014; pp. 3076–3083.
29. Wintrich, A.; Nicolai, U.; Tursky, W.; Reimann, T. *Application Manual—Power Semiconductors*; Semikron International GmbH: Nuremberg, Germany, 2011.
30. Behjati, H.; Davoudi, A. Reliability analysis framework for structural redundancy in power semiconductors. *IEEE Trans. Ind. Electron.* **2013**, *10*, 4376–4386. [\[CrossRef\]](#)
31. Musarrat, M.N.; Islam, M.R.; Muttaqi, K.; Sutanto, D.; Rahman, M.A. Improving the thermal performance of rotor-side converter of doubly-fed induction generator wind turbine while operating around synchronous speed. *IEEE J. Emerg. Sel. Top. Ind. Electron.* **2021**, *3*, 298–307. [\[CrossRef\]](#)
32. Zhou, D.; Blaabjerg, F. Optimized demagnetizing control of DFIG power converter for reduced thermal stress during symmetrical grid fault. *IEEE Trans. Power Electron.* **2018**, *33*, 10326–10340. [\[CrossRef\]](#)
33. Kovács, P.K. *Transient Phenomena in Electrical Machines*; Elsevier: Amsterdam, The Netherlands, 1984.
34. Pena, R.; Clare, J.; Asher, G. Doubly fed induction generator using back-to-back PWM converters and its application to variable-speed wind-energy generation. *IEE Proc.-Electr. Power Appl.* **1996**, *143*, 231–241. [\[CrossRef\]](#)
35. Rodriguez, P.; Teodorescu, R.; Candela, I.; Timbus, A.V.; Liserre, M.; Blaabjerg, F. New positive-sequence voltage detector for grid synchronization of power converters under faulty grid conditions. In Proceedings of the 2006 37th IEEE Power Electronics Specialists Conference, Jeju, Korea, 18–22 June 2006; pp. 1–7.
36. Mendes, V.F.; de Sousa, C.V.; Hofmann, W.; Silva, S.R. Doubly-fed induction generator ride-through fault capability using resonant controllers for asymmetrical voltage sags. *IET Renew. Power Gener.* **2015**, *9*, 783–791. [\[CrossRef\]](#)
37. Teodorescu, R.; Liserre, M.; Rodriguez, P. *Grid Converters for Photovoltaic and Wind Power Systems*; John Wiley & Sons: Hoboken, NJ, USA, 2011.
38. Hu, J.; He, Y. Modeling and enhanced control of DFIG under unbalanced grid voltage conditions. *Electr. Power Syst. Res.* **2009**, *79*, 273–281. [\[CrossRef\]](#)
39. Hu, J.; He, Y.; Xu, L.; Williams, B.W. Improved control of DFIG systems during network unbalance using PI-R current regulators. *IEEE Trans. Ind. Electron.* **2008**, *56*, 439–451. [\[CrossRef\]](#)
40. Hu, J.; He, Y. DFIG wind generation systems operating with limited converter rating considered under unbalanced network conditions—analysis and control design. *Renew. Energy* **2011**, *36*, 829–847. [\[CrossRef\]](#)
41. Liserre, M.; Teodorescu, R.; Blaabjerg, F. Multiple harmonics control for three-phase grid converter systems with the use of PI-RES current controller in a rotating frame. *IEEE Trans. Power Electron.* **2006**, *21*, 836–841. [\[CrossRef\]](#)
42. Lopez, J.; Sanchis, P.; Roboam, X.; Marroyo, L. Dynamic behavior of the doubly fed induction generator during three-phase voltage dips. *IEEE Trans. Energy Convers.* **2007**, *22*, 709–717. [\[CrossRef\]](#)
43. López, J.; Sanchis, P.; Gubía, E.; Ursúa, A.; Marroyo, L.; Roboam, X. Control of doubly fed induction generator under symmetrical voltage dips. In Proceedings of the 2008 IEEE International Symposium on Industrial Electronics, Cambridge, UK, 30 June–2 July 2008; pp. 2456–2462.
44. Bollen, M.H. *Understanding Power Quality Problems*; IEEE Press: Piscataway, NJ, USA, 2000.
45. Xu, L. Coordinated control of DFIG's rotor and grid side converters during network unbalance. *IEEE Trans. Power Electron.* **2008**, *23*, 1041–1049.
46. Lopez, J.; Gubia, E.; Sanchis, P.; Roboam, X.; Marroyo, L. Wind turbines based on doubly fed induction generator under asymmetrical voltage dips. *IEEE Trans. Energy Convers.* **2008**, *23*, 321–330. [\[CrossRef\]](#)
47. Infineon Datasheet of Module FF1500R12IE5. Available online: [https://www.infineon.com/dgdl/Infineon-FF1500R12IE5-DataSheet-v03\\_01-EN.pdf?fileId=5546d4625f2e26bc015f2e9197d90007](https://www.infineon.com/dgdl/Infineon-FF1500R12IE5-DataSheet-v03_01-EN.pdf?fileId=5546d4625f2e26bc015f2e9197d90007) (accessed on 20 April 2022).
48. SEMIKRON Datasheet of Heatsink P16/300. Available online: <https://pdf1.alldatasheetpt.com/datasheet-pdf/view/127115/SEMIKRON/P16/300.html> (accessed on 20 April 2022).
49. Infineon Datasheet of Module FF1500R17IP5P. Available online: [https://www.infineon.com/dgdl/Infineon-FF1500R17IP5P-DataSheet-v03\\_02-EN.pdf?fileId=5546d46264a8de7e0164f4b761db4512](https://www.infineon.com/dgdl/Infineon-FF1500R17IP5P-DataSheet-v03_02-EN.pdf?fileId=5546d46264a8de7e0164f4b761db4512) (accessed on 20 April 2022).